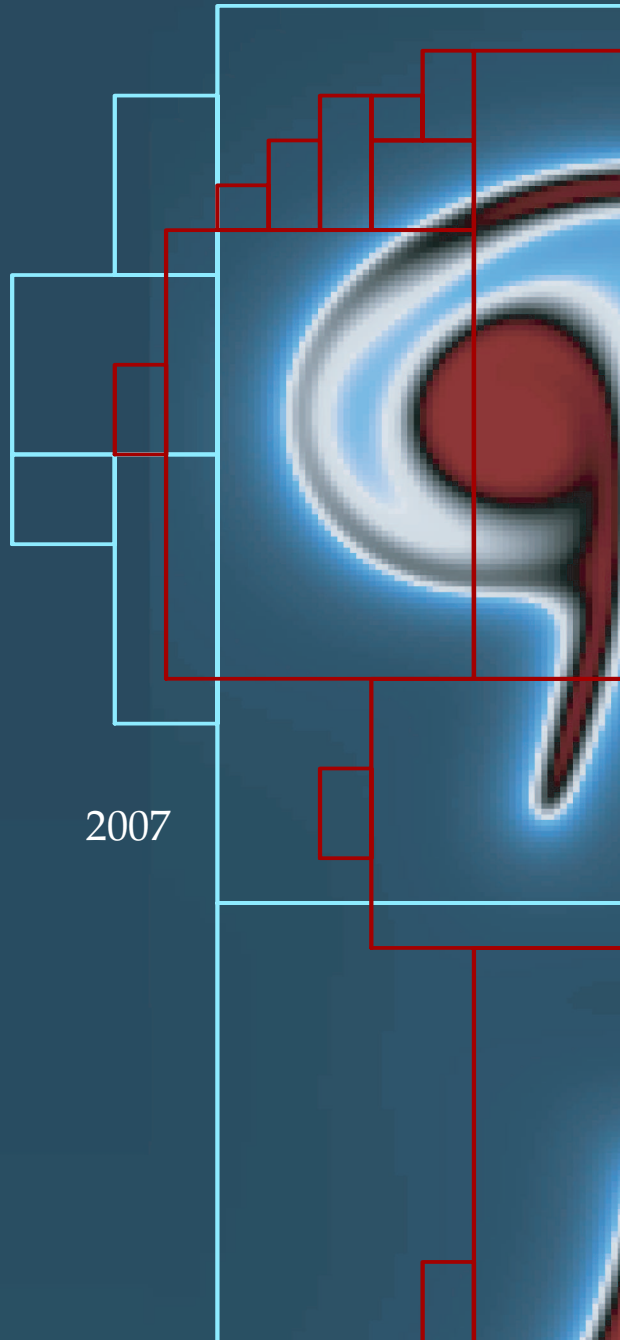


*Communications in
Applied
Mathematics and
Computational
Science*

Volume 2

No. 1

2007



**THE EXTENDED FINITE ELEMENT METHOD FOR
BOUNDARY LAYER PROBLEMS IN BIOFILM GROWTH**

BRYAN G. SMITH, BENJAMIN L. VAUGHAN JR. AND DAVID L. CHOPP



mathematical sciences publishers

THE EXTENDED FINITE ELEMENT METHOD FOR BOUNDARY LAYER PROBLEMS IN BIOFILM GROWTH

BRYAN G. SMITH, BENJAMIN L. VAUGHAN JR. AND DAVID L. CHOPP

In this paper, we use the eXtended Finite Element Method, with customized enrichment functions determined by asymptotic analysis, to study boundary layer behavior in elliptic equations with discontinuous coefficients. In particular, we look at equations where the coefficients are discontinuous across a boundary internal to the domain. We also show how to implement this method for Dirichlet conditions at an interface. The method requires neither the mesh to conform to the internal boundary, nor the mesh to have additional refinement near the interface, making this an ideal method for moving interface type problems. We then apply this method to equations for linearized biofilm growth to study the effects of biofilm geometry on the availability of substrate and the effect of tip-splitting in biofilm growth.

1. Introduction

Consider the equation

$$\nabla \cdot (\beta \nabla u) + \kappa u = f, \tag{1}$$

on a two-dimensional domain, Ω , containing an interface Γ . The coefficients β , κ , and f may be discontinuous across Γ , leading to discontinuities in the normal derivative of the solution, u . In addition, large variations between these coefficients can lead to the existence of boundary layers near the interface, particularly when β is small relative to κ or f .

This type of equation governs a wide range of physical processes, and thus a variety of numerical methods have been devised to solve it. The three most commonly used approaches are finite difference methods — such as those described in [9; 11; 14] — finite element methods, and boundary element methods. One method that has been shown to perform well in comparisons with other methods is

MSC2000: 65N30, 92B05.

Keywords: X-FEM, extended finite element method, level set method, elliptic equations, Helmholtz equation, biofilms.

Smith was supported in part by the DoD NDSEG Fellowship Program and the Chicago Chapter of the ARCS Foundation. Vaughan and Chopp were supported in part by a grant from the NIH under contract #R01- GM067248.

the eXtended Finite Element Method (X-FEM) [8; 16]. In fact, it was shown in [12] that this method produced significantly more accurate solutions near the interface Γ . The X-FEM is a partition of unity method [15] in which extra functions containing information about the location of an interface are added to the standard finite element approximation. The method is particularly suited to problems involving a moving interface, since it does not require a conforming mesh, and can be easily coupled to interface tracking methods such as the level set method [17].

The X-FEM has been used to model crack growth [7; 16; 18; 20], solidification [3; 10], arbitrary fixed material interfaces and voids [19], rigid particles in Stokes flow [21], and multiphase fluids [2]. The majority of this work has relied on generic enrichment functions, such as Heaviside or absolute value functions, to enforce interfacial boundary conditions. However, in [7], it was shown that a special enrichment function given by the exact near-tip asymptotic functions, could be added to the approximation at the crack tip to improve accuracy. In this paper, we show how the X-FEM can be used to efficiently model systems that exhibit boundary layer behavior at the interface by expanding the function space with customized enrichment functions along the entire interface, presenting as an example a new exponential enrichment function that captures solutions which grow or decay rapidly near the interface.

The application to which we apply this method concerns the growth of biofilms. Biofilms are microbial communities that grow attached to solid surfaces, and are one of the most ubiquitous forms of life on the planet. More than 90% of all bacteria live in biofilms [1]. Biofilms are used in wastewater treatment and bioremediation of contaminated soils, lakes, and rivers. Biofilms also cause disease in plants and animals, and damage pipes, heat exchangers, and ship hulls. Consequently, understanding biofilms is important for a wide range of health and engineering disciplines. The work we present here is toward a goal of building continuum level model tools for simulating biofilm growth and development.

In this paper, we solve the linearized biofilm growth equations in order to determine how the geometry of the colony affects the profile of its growth, addressing two specific phenomena: fingering growth due to a tip-splitting instability and the shadowing effect generated by large colonies.

2. Numerical method

The eXtended Finite Element method (X-FEM) is a modified finite element method used for approximating the solution to (1). However, unlike conventional finite element methods, the X-FEM does not require the mesh to conform to the interface geometry, allowing us to utilize a standard Cartesian mesh. This is particularly

useful in problems involving moving interfaces, due to the fact that the mesh does not have to be regenerated at each timestep.

The X-FEM avoids the need for a conforming mesh by supplementing the standard finite element functions with enrichment functions that contain information about the interface. The X-FEM approximation for the solution u is written as

$$u^h(x, y) = \sum_{n_i \in N} \phi_i(x, y) u_i + \sum_k \sum_{n_j \in N_E} \phi_j(x, y) \psi_k(\varphi) a_j, \quad (2)$$

where N is the set of all nodes in the domain, N_E is the set of enriched nodes, ϕ is a standard finite element test function, ψ_k is the enrichment function, and φ is the signed distance function representing the interface.

Here we describe only the construction of the enrichment functions as well as the application of boundary conditions. A detailed treatment of the full X-FEM implementation is found in [12].

2.1. Determining enrichment functions. The enrichment functions added to the standard finite element approximation in the X-FEM serve two purposes. First, they encode the location of the interface into the function space itself, which allows for the application of both Dirichlet and Neumann interface conditions without the need for a conforming mesh. Second, they may contain information about the asymptotic behavior of the solution near the interface, allowing the method to accurately capture boundary layer behavior without the need for a very fine mesh. Here we test three types of enrichment functions. The first two, the step enrichment and the absolute value enrichment, are generic enrichment functions that can be applied to any problem that is continuous across the interface. The third, the exponential enrichment, is a custom enrichment function that is tailored to problems that display exponential behavior within the interfacial boundary layer. Each enrichment is a function only of the signed distance from the interface:

$$\varphi = \pm \min_{X \in \Gamma} \|x - X\|,$$

where the sign depends on whether x is inside or outside the region enclosed by the interface Γ . This signed distance function is typically determined using the Level Set Method [17].

The step and absolute value enrichment functions are defined as

$$\psi_{\text{step}}(\varphi) = \begin{cases} 1 & \varphi > 0, \\ -1 & \varphi \leq 0, \end{cases}$$

and

$$\psi_{\text{abs}}(\varphi) = \begin{cases} \varphi & \text{if } \varphi > 0, \\ -\varphi & \text{if } \varphi \leq 0. \end{cases}$$

These are simple enrichment functions that can be implemented without any *a priori* knowledge of solution behavior near the interface.

The exponential enrichment function is defined as

$$\psi_{\text{exp}}(\varphi) = \begin{cases} 1 - e^{\mu\varphi} & \text{if } \varphi > 0, \\ -\varphi & \text{if } \varphi \leq 0. \end{cases}$$

This enrichment is most effective when asymptotic analysis indicates the presence of a boundary layer which exhibits exponential behavior. The value of the parameter μ depends on the specific parameters of the problem. It is important to note that both the absolute value and exponential enrichments decay to zero at the interface. This condition is necessary for stability when a nonzero Dirichlet condition is applied at the interface.

While the X-FEM has traditionally only added enrichment functions to elements containing the interface, it can be advantageous to enrich beyond this layer of elements when using enrichment functions other than the step enrichment. This is particularly important when using a custom enrichment because it allows the enrichment function to be applied throughout the boundary layer, thus capturing the behavior more completely. In the case of the absolute value enrichment, extending the enrichment distance effectively increases the order of the finite element approximation in the critical region near the interface. It is also useful to enrich to a different distance on either side of the interface when the enrichment function is asymmetric. As it is difficult to determine the optimal enrichment distance analytically, trial and error is generally the best method. For the problems presented here, an enrichment distance of $\mu \log 10^{-3}$ is used for exponential functions and $\mu \log 10^{-2}$ is used for linear functions. These correspond to the distance it takes the function $e^{\mu\varphi}$ to decay to 10^{-3} and 10^{-2} respectively.

2.2. Interface conditions. Once the enrichment function has been determined, the next consideration is the proper application of the boundary conditions. Here we only consider problems which are continuous across the interface, so there are two types of conditions that can be applied: Dirichlet conditions, $u = h(x, y)$, and Neumann jump conditions, $[[\beta\hat{n} \cdot \nabla u]] = v(x, y)$, where $[[\cdot]]$ indicates the jump across Γ .

Neumann jump conditions. The Neumann jump condition is enforced primarily by introducing a line source term to the right hand side of (1). This line source has strength $v(x, y)$ and is written as

$$\int_{\Gamma} v(x, y) \delta(x - X(s)) d\Gamma, \quad (3)$$

where $X(s)$ is the parameterized interface.

This technique can be used with both continuous and discontinuous enrichment functions and typically yields the best results with the Step enrichment. However, approximations using continuous enrichment functions can also utilize Lagrange multipliers to enforce jump conditions. In this case, the governing equation is rewritten as

$$\nabla \cdot (\beta \nabla u) + \kappa u + \left[\left[\beta \frac{\partial u}{\partial n} \right] \right] \lambda = f + \int_{\Gamma} v(x, y) \delta(x - X(s)) d\Gamma,$$

along with the condition

$$\left[\left[\beta \hat{n} \cdot \nabla u \right] \right] = v(x, y).$$

A one dimensional finite element mesh is laid down on the interface using piecewise linear elements, and the Lagrange multipliers are approximated by:

$$\lambda^h = \sum_{m_i \in M} \theta_i \lambda_i,$$

where M is the set of all Lagrange multiplier nodes.

Dirichlet conditions. Dirichlet conditions on an internal interface have not been considered in previous implementations of the X-FEM. This type of condition is unusual because it divides the domain into two independent pieces, which are typically solved separately. However, in order to avoid the generation of meshes which conform to each piece, it can be useful to solve on the whole domain at once.

In contrast to the derivative jump conditions, Dirichlet interface conditions can only be applied using Lagrange multipliers. This is done in a similar manner as above, with the governing equation rewritten to include the extra terms:

$$\nabla \cdot (\beta \nabla u) + \kappa u + \lambda u|_{\Gamma} = f,$$

with the condition

$$u|_{\Gamma} = h(x, y).$$

For systems with continuous enrichment functions, only one set of Lagrange multipliers is necessary to apply the boundary condition. Discontinuous enrichments, however, do not have a single value at the interface, so the condition must be applied to the positive and negative sides separately, requiring two sets of Lagrange multipliers.

2.3. Evaluation of interface derivatives. In order to accurately determine the derivative jump across the interface, a domain integral method, similar to the one described in [8], is employed. We first consider a section of interface, Γ_i , within the support, Ω_i , of a test function ϕ_i . Equation (1) is multiplied by ϕ_i and integrated

over Ω_i . Integrating by parts yields

$$\int_{\Omega_i} (-\beta \nabla u \cdot \nabla \phi_i + \kappa u \phi_i - f \phi_i) d\Omega_i = \int_{\Gamma_i} [[\beta \hat{n} \cdot \nabla u]]_{\Gamma_i} \phi_i d\Gamma_i. \quad (4)$$

Using a first order approximation, the derivative jump is assumed to be constant along Γ_i . Equation (4) can then be rewritten as

$$[[\beta \hat{n} \cdot \nabla u]]_{\Gamma_i} = \frac{1}{\int_{\Gamma_i} \phi_i d\Gamma_i} \int_{\Omega_i} (-\beta \nabla u \cdot \nabla \phi_i + \kappa u \phi_i - f \phi_i) d\Omega_i. \quad (5)$$

To then determine the jump at a single point on the interface, x_d , the jump across the interface segment is determined using each test function, ϕ_i , which has support containing x_d . In order to avoid oscillations due to roundoff error, interface segments are discarded if the integral of ϕ_i over the segment is less than 10^{-13} . These values are then weighted appropriately and summed:

$$[[\beta \hat{n} \cdot \nabla u]]_{x_d} = \sum_j [[\beta \hat{n} \cdot \nabla u]]_{\Gamma_j} \phi_j(x_d).$$

3. Results

In this section, different types of enrichment functions are applied to the solution of two example problems. In each problem, exponential enrichment functions are compared to both absolute value enrichments and step enrichments when finding a solution that contains a boundary layer. For each problem the interface Γ is the circle $(x - \frac{1}{2})^2 + (y - \frac{1}{2})^2 = \frac{1}{16}$ within the domain $0 \leq x, y \leq 1$.

We solve each example problem using both types of interface conditions discussed in Section 2.2. These two types of boundary conditions demonstrate how the custom enrichment function can improve the accuracy of both the solution and its derivative at the interface.

3.1. Example 1: enriching with the exact solution. The first example shows the improvement in the finite element approximation when the exact solution is included in the enriched function space. The differential equation is

$$\nabla^2 u + \frac{\kappa}{\epsilon} \left(\frac{1}{\epsilon} - \frac{1}{r} \right) u = 0, \quad (6)$$

where

$$\kappa(x, y) = \begin{cases} 0 & \text{if } r \leq \frac{1}{4}, \\ 1 & \text{if } r > \frac{1}{4}. \end{cases}$$

The exact solution to (6) is

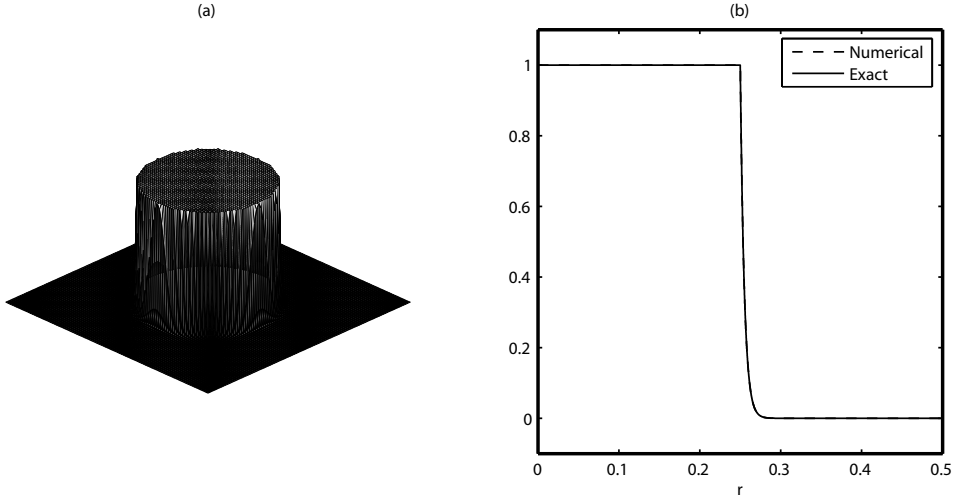


Figure 1. Solution of Example 1. (a) A surface plot of the solution on the entire domain. (b) A cross section of the solution, taken at an angle of one radian. The numerical approximation overlaps the exact solution and is computed using the exponential enrichment function on a 799×799 grid.

$$u(x, y) = \begin{cases} 1 & \text{if } r \leq \frac{1}{4}, \\ \exp\left[\frac{1}{\epsilon}\left(\frac{1}{4} - r\right)\right] & \text{if } r > \frac{1}{4}, \end{cases}$$

where ϵ is $\frac{1}{200}$. The expression $\frac{1}{4} - r$ is equivalent to the level set variable φ , so the exact solution on the exterior of the circle is contained within the exponential enrichment function.

Equation (6) is solved with two sets of boundary conditions. The first prescribes continuity and sets a derivative jump condition on Γ :

$$\llbracket u \rrbracket = 0, \quad \left[\left[\frac{\partial u}{\partial n} \right] \right] = \frac{1}{\epsilon}.$$

Because the derivative jump along the interface is already known, the important simulation results to consider are the solution values along the interface and throughout the domain.

Table 1 shows the convergence results for the X-FEM using three types of enrichment functions: the step enrichment, absolute value enrichment, and exponential enrichment. The error given is the maximum error at the nodes, defined as

$$\|T_n\|_\infty = \max_{n_i \in N} \{|u(x_i, y_i) - u_i^h|\},$$

n	Step		Absolute Value		Exponential	
	$\ T_n\ _\infty$	ratio	$\ T_n\ _\infty$	ratio	$\ T_n\ _\infty$	ratio
49	1.3367×10^{-1}		2.8126×10^{-1}		3.6922×10^{-2}	
99	7.8584×10^{-2}	1.701	4.9647×10^{-2}	5.665	8.1788×10^{-3}	4.514
199	2.6213×10^{-2}	2.998	9.8545×10^{-3}	5.038	1.8534×10^{-3}	4.413
399	8.5907×10^{-3}	3.051	3.5610×10^{-3}	2.760	4.6404×10^{-4}	3.994
799	2.9094×10^{-3}	2.953	9.7458×10^{-4}	3.663	1.1565×10^{-4}	4.013

Table 1. Domain results for Example 1 with Neumann jump interface conditions.

where N is the set of all nodes, (x_i, y_i) is the location of the i -th node, and u_i^h is the computed value at the node. The ratios of successive errors are included as well to show convergence rates. As Table 1 shows, the exponential enrichment is more accurate than both the absolute value and step enrichments, and it converges more uniformly as well.

Of greater importance for moving interface problems is the accuracy of the solution at the interface. This can be problematic for some methods even though they exhibit good accuracy away from the interface [12]. Table 2 shows the error interpolated along the interface. This error is computed at 1,000 evenly spaced points along the parameterized interface. The results are similar to those seen in Table 1, but the disparity between the exponential enrichment and the other enrichments is more significant.

The second boundary condition we consider is a Dirichlet condition on both sides of the interface:

$$u = 1.$$

n	Step		Absolute Value		Exponential	
	$\ T_n\ _\infty$	ratio	$\ T_n\ _\infty$	ratio	$\ T_n\ _\infty$	ratio
49	3.4331×10^{-1}		4.5436×10^{-1}		3.6860×10^{-2}	
99	1.4444×10^{-1}	2.377	1.3363×10^{-1}	3.400	9.1137×10^{-3}	4.045
199	3.9447×10^{-2}	3.662	4.5511×10^{-2}	2.936	1.9652×10^{-3}	4.638
399	1.1170×10^{-2}	3.531	1.4101×10^{-2}	3.228	5.3682×10^{-4}	3.661
799	3.1200×10^{-3}	3.580	3.6471×10^{-3}	3.866	1.3277×10^{-4}	4.043

Table 2. Interface results for Example 1 with Neumann Jump interface conditions.

n	Step		Absolute Value		Exponential	
	$\ T_n\ _\infty$	ratio	$\ T_n\ _\infty$	ratio	$\ T_n\ _\infty$	ratio
49	2.5623×10^{-2}		1.9174×10^{-1}		1.1620×10^{-2}	
99	2.2492×10^{-2}	1.135	6.9352×10^{-2}	2.765	4.4235×10^{-3}	2.627
199	1.4385×10^{-2}	1.564	2.1398×10^{-2}	3.241	8.7237×10^{-4}	5.071
399	6.0928×10^{-3}	2.361	5.9632×10^{-3}	3.588	3.1170×10^{-4}	2.799
799	1.9458×10^{-3}	3.131	1.5402×10^{-3}	3.872	6.0066×10^{-5}	5.189

Table 3. Domain results for Example 1 with Dirichlet interface conditions.

The exact solution remains the same as above. Here, the value at the interface is known, so the important computational results are the solution values within the domain and the jump in the derivative across the interface.

Table 3 contains the convergence results for the X-FEM using this boundary condition. Once again, the asymptotic enrichments perform much better than the other two, by more than an order of magnitude. Table 4 shows the gradient results on the interface. Due to the magnitude of the gradient jump ($\sim 10^2$), this table presents relative errors rather than absolute errors:

$$\|T'_n\|_\infty = \frac{1}{1/\epsilon} \max_{n_i \in N} \{|u(x_i, y_i) - u_i^h|\}.$$

3.2. Example 2: enriching with an asymptotic solution. In the second example, the custom enrichment function does not contain the exact solution, but instead includes the asymptotic approximation of the solution near the interface. The equation in this example is the Helmholtz Equation on the interior of a circle with radius $\frac{1}{4}$:

n	Step		Absolute Value		Exponential	
	$\ T'_n\ _\infty$	ratio	$\ T'_n\ _\infty$	ratio	$\ T'_n\ _\infty$	ratio
49	4.2738×10^{-1}		2.2663×10^{-1}		3.1433×10^{-2}	
99	1.9041×10^{-1}	2.245	9.1789×10^{-2}	2.469	1.5427×10^{-2}	2.038
199	6.8870×10^{-2}	2.765	3.4742×10^{-2}	2.642	3.8923×10^{-3}	3.964
399	3.1636×10^{-2}	2.177	1.7591×10^{-2}	1.975	1.4946×10^{-3}	2.604
799	1.3817×10^{-2}	2.290	8.5566×10^{-3}	2.056	5.5810×10^{-4}	2.678

Table 4. Interfacial gradient results for Example 1 with Dirichlet interface conditions.

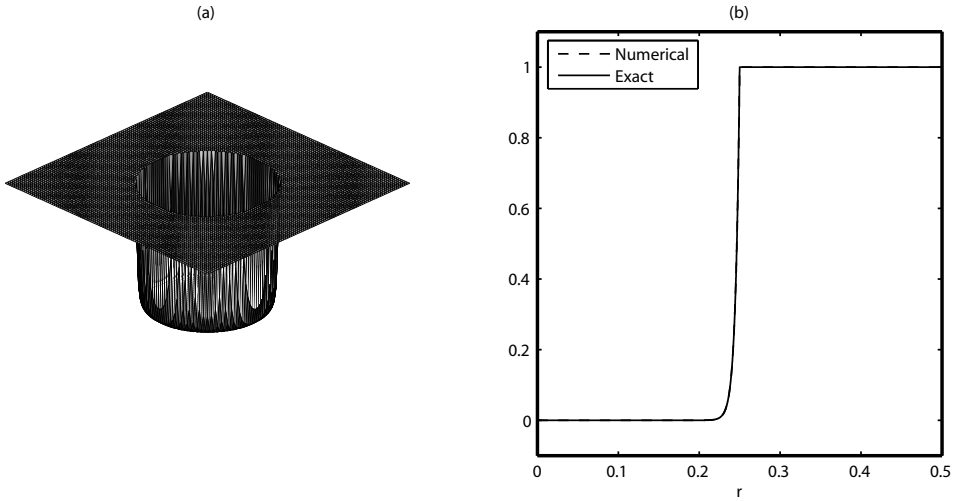


Figure 2. Solution of Example 2. (a) A surface plot of the solution on the entire domain. (b) A cross section of the solution, taken at an angle of one radian. The numerical approximation overlaps the exact solution and is computed using the exponential enrichment function on a 799×799 grid.

$$\nabla^2 u + \kappa^2 u = 0, \quad (7)$$

where κ is given by

$$\kappa(x, y) = \begin{cases} 200 & \text{if } r \leq \frac{1}{4}, \\ 0 & \text{if } r > \frac{1}{4}. \end{cases}$$

The exact solution to (7) is

$$u(x, y) = \begin{cases} \frac{I_0(\kappa r)}{I_0(\frac{\kappa}{4})} & \text{if } r \leq \frac{1}{4}, \\ 1 & \text{if } r > \frac{1}{4}, \end{cases}$$

where $I_n(x)$ is the modified Bessel function of the first kind.

An asymptotic analysis of (7) shows that the behavior of the solution in the boundary layer near the interface is of the form $u \approx e^{\kappa r}$. Therefore, the exponential enrichment function is appropriate here as well, using κ as the parameter. It is important to note that while an exact solution to (7) is available, we only use information from the asymptotic analysis to construct our approximation.

As in Example 1, we once again consider two types of interface conditions. First, the solution is again prescribed to be continuous, with a jump in the normal

n	Step		Absolute Value		Exponential	
	$\ T_n\ _\infty$	ratio	$\ T_n\ _\infty$	ratio	$\ T_n\ _\infty$	ratio
49	1.6496×10^{-1}		2.8971×10^{-1}		1.8642×10^{-2}	
99	7.7465×10^{-2}	2.130	5.8281×10^{-2}	4.971	5.4660×10^{-3}	3.429
199	2.8396×10^{-2}	2.728	1.1361×10^{-2}	5.130	1.5259×10^{-3}	3.582
399	8.8436×10^{-3}	3.211	2.4660×10^{-3}	4.607	3.8795×10^{-4}	3.933
799	2.8451×10^{-3}	3.108	8.1249×10^{-4}	3.035	9.7831×10^{-5}	3.966

Table 5. Domain results for Example 2 with Neumann jump interface conditions.

derivative at the interface:

$$[[u]] = 0, \quad \left[\left[\frac{\partial u}{\partial n} \right] \right] = \kappa \frac{I_1(\kappa r)}{I_0\left(\frac{\kappa}{4}\right)}.$$

Table 5 shows the error on the domain, and Table 6 shows the error on the interface. The results are similar to those in the Example 1.

Like the first example, the second set of boundary conditions applies a Dirichlet condition at the interface, and the solution gradient at the interface is the desired result:

$$u = 1.$$

Table 7 shows that the asymptotic enrichment again outperforms the other generic enrichment functions with an error of less than 0.1% for the largest system. For the sake of completeness, Table 8 charts the maximum error on the domain.

Finally, the exponential enrichment function not only increases the accuracy at the nodes and the interface, it improves the approximation within the elements as well. Because the asymptotic solution is contained in the interpolant, fewer

n	Step		Absolute Value		Exponential	
	$\ T_n\ _\infty$	ratio	$\ T_n\ _\infty$	ratio	$\ T_n\ _\infty$	ratio
49	3.2720×10^{-1}		3.6044×10^{-1}		3.4735×10^{-2}	
99	1.2621×10^{-1}	2.593	1.1859×10^{-1}	3.040	7.1808×10^{-3}	4.837
199	3.9873×10^{-2}	3.165	4.0367×10^{-2}	2.938	1.9359×10^{-3}	3.709
399	1.0574×10^{-2}	3.771	1.2436×10^{-2}	3.246	4.9710×10^{-4}	3.887
799	2.9643×10^{-3}	3.567	3.3563×10^{-3}	3.705	1.2127×10^{-4}	4.106

Table 6. Interface results for Example 2 with Neumann jump interface conditions.

n	Step		Absolute Value		Exponential	
	$\ T'_n\ _\infty$	ratio	$\ T'_n\ _\infty$	ratio	$\ T'_n\ _\infty$	ratio
49	3.5875×10^{-1}		2.3265×10^{-1}		3.6010×10^{-2}	
99	1.5830×10^{-1}	2.266	9.0700×10^{-2}	2.565	1.6945×10^{-2}	2.125
199	5.7291×10^{-2}	2.763	4.0960×10^{-2}	2.214	4.0448×10^{-3}	4.189
399	2.4665×10^{-2}	2.323	1.8754×10^{-2}	2.184	1.6265×10^{-3}	2.487
799	1.2950×10^{-2}	1.905	9.9692×10^{-3}	2.067	5.9443×10^{-4}	2.736

Table 7. Interface gradient results for Example 2 with Dirichlet interface conditions.

n	Step		Absolute Value		Exponential	
	$\ T_n\ _\infty$	ratio	$\ T_n\ _\infty$	ratio	$\ T_n\ _\infty$	ratio
49	3.0534×10^{-2}		1.3923×10^{-1}		6.6740×10^{-3}	
99	2.2035×10^{-2}	1.386	6.1419×10^{-2}	2.267	3.1346×10^{-3}	2.129
199	1.4526×10^{-2}	1.517	1.6752×10^{-2}	3.666	7.4375×10^{-4}	4.215
399	6.6449×10^{-3}	2.186	4.8119×10^{-3}	3.481	2.8600×10^{-4}	2.601
799	2.0239×10^{-3}	3.283	1.2758×10^{-3}	3.772	5.6394×10^{-5}	5.071

Table 8. Domain results for Example 2 with Dirichlet interface conditions.

elements are needed to capture the boundary layer. Figure 3 shows the exact solution plotted next to the numerical approximation for varying mesh sizes. Each plot is generated by evaluating the exact solution and the numerical approximation at 10,000 points along a line from $r = 0.23$ to $r = 0.26$ at an angle of one radian. This clearly demonstrates the advantage of using a customized enrichment function, as the exponential enrichment accurately approximates the solution on a 25×25 grid, where the entire boundary layer is contained within one element.

4. Biofilm growth

We now consider the problem of bacterial biofilms. The addition of substrate nutrients to the top of the film drives the growth of the biofilm. Here we explore how the geometry of the biofilm colonies affects the profile of their growth. We first consider the phenomenon of tip-splitting [4], where the colony does not grow directly toward the substrate, but develops fingers that grow at an angle into the film. We then analyze how the shadowing effect of a large colony decays with distance.

The system is considered on a domain Ω , periodic in x and consisting of two regions, the interior of the bacterial colonies, Ω_b , and the exterior fluid film, Ω_f .

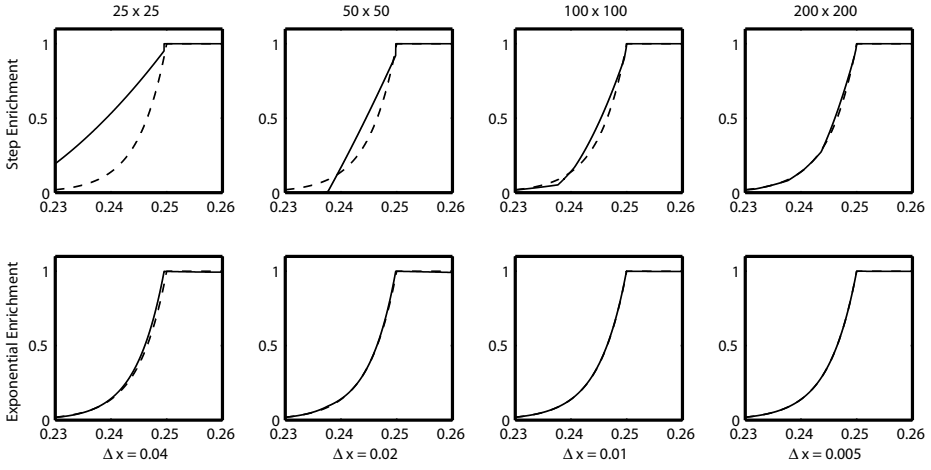


Figure 3. Cross sections generated using various mesh sizes. Each cross section is taken at an angle of one radian, to avoid alignment with the mesh. Note that in the coarsest plot, the entire boundary layer is contained in one element.

The substrate concentration s and velocity potential φ are governed by

$$D\nabla^2 s = \alpha s \quad (8)$$

and

$$\nabla^2 \varphi = \beta s, \quad (9)$$

where

$$D(x, y) = \begin{cases} 120 & \text{if } (x, y) \in \Omega_b, \\ 150 & \text{if } (x, y) \in \Omega_f, \end{cases}$$

$$\alpha(x, y) = \begin{cases} 3.6 \times 10^6 & \text{if } (x, y) \in \Omega_b, \\ 0 & \text{if } (x, y) \in \Omega_f, \end{cases}$$

and

$$\beta(x, y) = \begin{cases} 10^6 & \text{if } (x, y) \in \Omega_b, \\ 0 & \text{if } (x, y) \in \Omega_f. \end{cases}$$

Figure 4 shows the boundary conditions applied to each equation. This follows the description given in [6] without erosion, with the parameters chosen to approximate the behavior of the nonlinear system described in [5]. Both the substrate concentration and the velocity potential are continuous throughout the domain. In the substrate equation, a derivative jump condition is applied at the interface between the colony and the liquid, and in the velocity equation, a Dirichlet condition

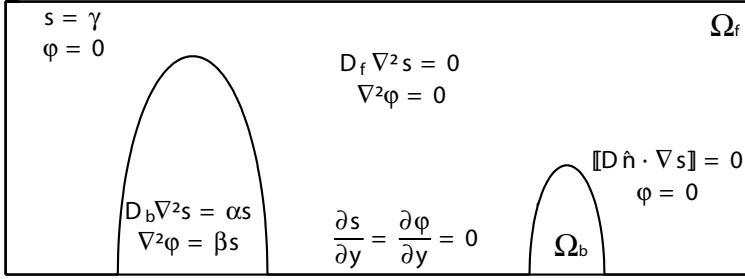


Figure 4. The domain and governing equations for the biofilm problem.

is prescribed:

$$[[D\hat{n} \cdot \nabla s]] = 0, \quad \varphi = 0.$$

In both cases, a Dirichlet condition is applied at the top boundary:

$$s = 10^{-5}, \quad \varphi = 0,$$

and a Neumann condition is applied at the bottom:

$$\frac{\partial s}{\partial y} = \frac{\partial \varphi}{\partial y} = 0.$$

We solve for the growth rate profile for a given colony via a three step process. First, the substrate concentration is found by solving (8) with the given boundary conditions. This solution is then fed back into (9) to find the velocity potential within the colony, and finally the rate of growth at the biofilm surface is given by the normal derivative of the velocity potential at the interface, $\hat{n} \cdot \nabla \varphi$. We calculate this quantity at a large number of points along the parameterized interface to obtain an overall profile of the colony's growth. Both the substrate and velocity equations are solved using the X-FEM with the exponential enrichment function. The relevant boundary layer exists on the interior of the colony, and we use $\mu = \sqrt{\alpha/D_b}$ as the parameter in the exponential enrichment definition.

4.1. Tip splitting. As biofilm colonies grow, they do not always grow in a uniform fashion. Sometimes the tip of the colony splits into separate fingers instead [4]. This instability appears to be distinct from the fingering instability described in [6], where it is observed that peaks have a greater growth rate than valleys. Due to random fluctuations, one of the fingers generally overtakes the other resulting in an irregularly shaped colony. The conditions driving this instability are unknown, but a possible mechanism is the splitting of a mushroom-shaped tip due to the instability described in [6]. This is similar to the well known tip-splitting instability in the Stefan problem, where a flattened dendritic tip splits due to the Mullins-Sekerka

instability [13]. Here we look at the ways in which the shape of a biofilm colony can lead to mushrooming of the tip.

To study the onset of mushrooming, we examine the velocity profiles of individual colonies on a periodic domain. The period of the domain is large enough to prevent interaction between neighboring colonies, and all of the colonies are hemielliptical in shape. Due to this simple geometry, the interface is easily parameterized from 0 to π , and Figure 5 shows some examples of parameterized velocity profiles. In the first case, the biofilm has an aspect ratio (height/width) of 2.25, and the maximum velocity is obtained at the peak of the biofilm colony, precluding a change in the shape of the tip. In the second case, the colony is much taller and thinner, with an aspect ratio of 16, and the maximum velocity is obtained on either side of the peak, which may allow for mushrooming to take place. Thus, to determine whether or not mushrooming can occur, we consider the ratio of the maximum velocity to the peak velocity. If this ratio is one, the maximum occurs at the peak, and the colony will grow normally. The strength of the mushrooming instability increases as this ratio moves above unity.

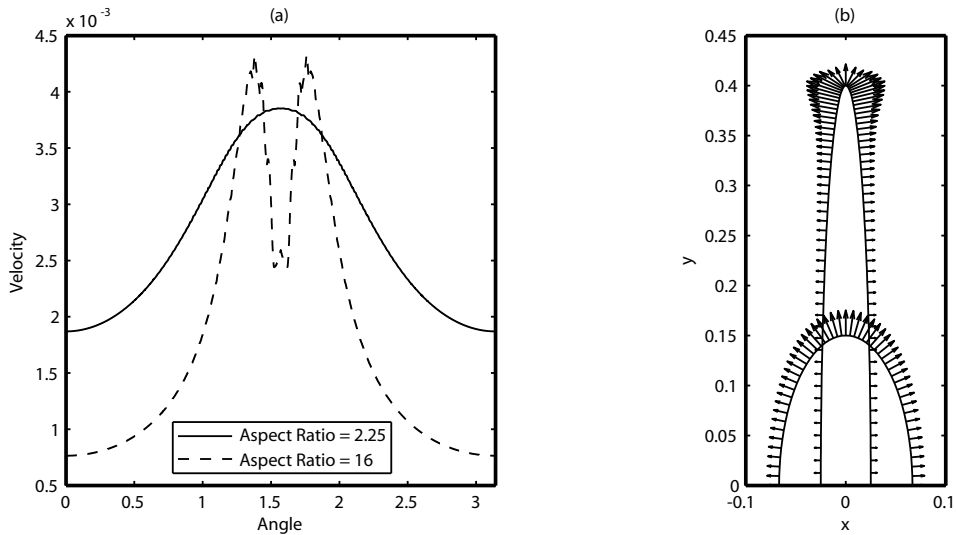


Figure 5. Representative velocity profiles. Shown here are two examples of velocity profiles, from colonies with different aspect ratios but the same mass. (a) Normal velocity vs. surface parameterization. In the second case, the maximum velocity is not attained at the tip, so mushrooming may occur. (b) Velocity vectors along the biofilm surface. The taller colony has a large aspect ratio, and the shape of the velocity field near the peak indicates that mushrooming may occur.

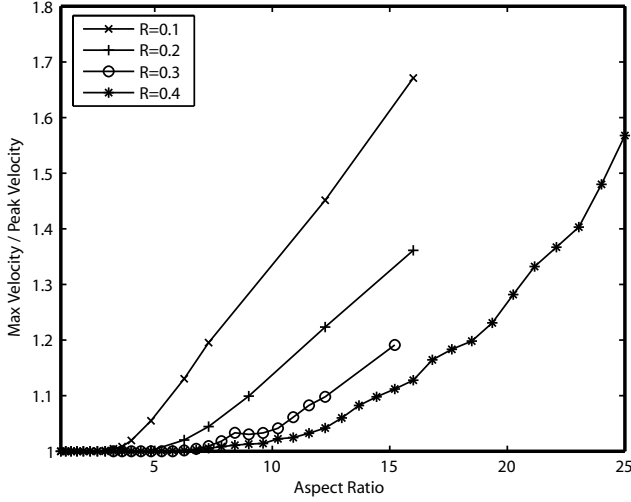


Figure 6. The effect of aspect ratio on mushrooming.

To demonstrate, we first explore how the aspect ratio of the hemielliptical colony affects the velocity profile. As we change the aspect ratio, we keep the area of the colony constant so that the total amount of biomass is unchanged. The colony shape is defined as

$$a^2(x - x_0)^2 + \frac{y^2}{a^2} = R^2,$$

where a^2 is the aspect ratio of the ellipse, and $R^2/2$ is the area. We vary the aspect ratio between 1.0 to 25.0 (height to width) for colonies with three different masses.

Figure 6 shows the relationship between the aspect ratio and the strength of the mushrooming instability. While the curves are qualitatively similar, the mass of the colony is clearly important. This mass effect can be removed by considering the radius of curvature at the colony peak, R/a^3 , rather than the aspect ratio. Figure 7 contains the same velocity data as Figure 6 but plotted against the radius of curvature. In this case, all three curves lie on top of each other, indicating that tip splitting is a function of the radius of curvature at the tip of the colony. So that we may ensure that other factors are not also important, the height of the film and the period of the domain were varied. As Figure 8 shows, these variations have no effect.

This dependence on radius of curvature is probably due to elevated substrate concentrations within the biofilm colony. As the tip radius decreases, less biomass is present near the peak, and unconsumed substrate can diffuse farther down into the colony. To quantify the substrate penetration, we calculate the depth within the colony at which the concentration of substrate is 10% of the concentration at the colony tip. In order to compare biofilms containing different amounts of biomass, we normalize all of the values by the substrate penetration depth into a circular

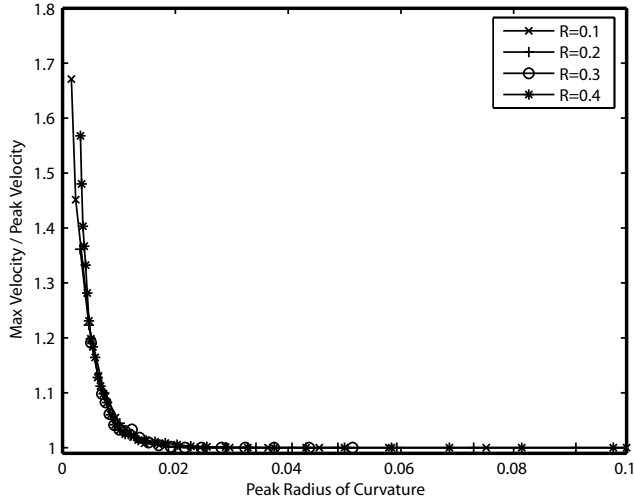


Figure 7. The effect of radius of curvature on mushrooming.

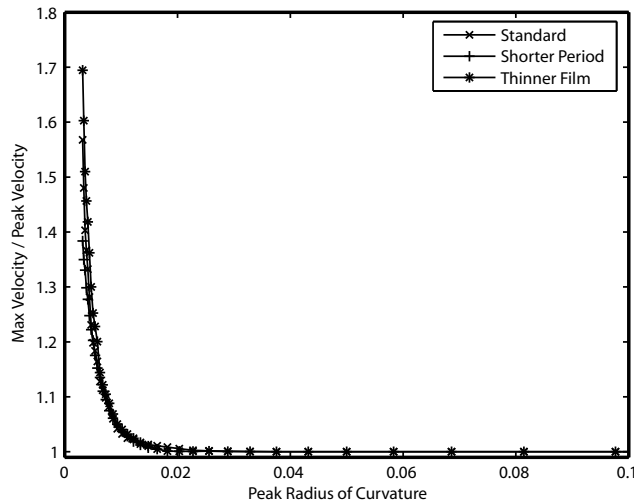


Figure 8. Domain period and film thickness have no effect on mushrooming.

colony with radius R . As shown in Figure 9, the substrate penetration depth is correlated with the radius of curvature.

4.2. Shadowing. Another important feature of biofilm growth is the interaction between neighboring colonies. Competition for substrate creates a shadowing effect near large colonies as nearby colonies are unable to attain their optimal growth rate. This shadowing effect depends on the relative sizes of the colonies as well as the separation distance. In order to determine the relative importance of these two

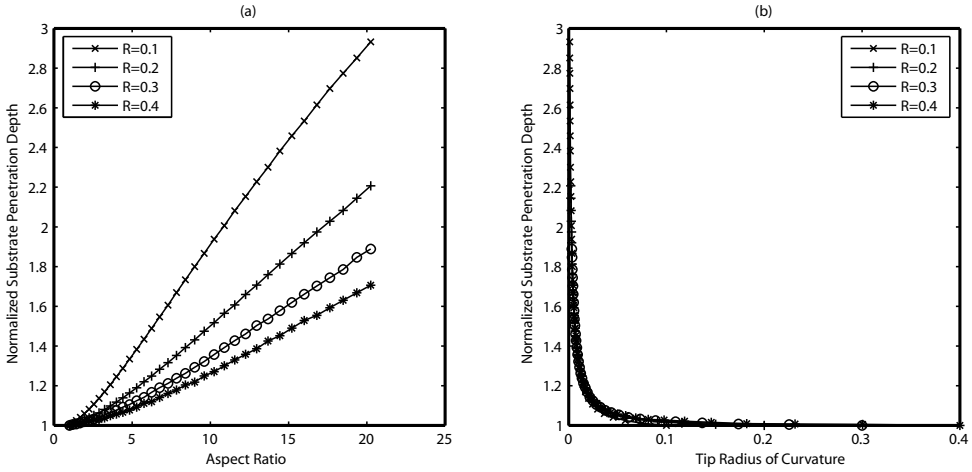


Figure 9. Normalized substrate penetration depths. (a) The normalized penetration depths for colonies of various sizes against the aspect ratio of the colony. (b) The normalized penetration depths against the radius of curvature at the colony tip.

parameters, we consider a system consisting of alternating large and small colonies along a periodic domain. In each case the large colony remains a standard size, with $a = 2.0$ and $R = 0.2$. The smaller colony maintains the same aspect ratio, but R is varied from 0.02 to 0.18. The different size cases are then simulated using a wide range of period lengths.

Proper determination of the effects of the interaction requires the maximum growth rate of an uninfluenced single colony, the natural growth rate for that colony. Due to the fact that the majority of a biofilm colony's growth occurs at or near the tip, this maximum growth rate is a reasonable measure of the overall growth rate of the colony. To find this rate, simulations are performed using a single colony on a periodic domain, using the same film height as in the combined system. The period of the domain is increased until maximum growth rate asymptotes to a constant value. Figure 10 shows maximum growth rate plotted against the period size for several representative colony sizes. Interestingly, the maximum growth rate of the smallest colonies is greater than that of the medium sized colonies. This effect is caused by mushrooming. When the colonies are relatively large, growth occurs primarily at the tip, and therefore the maximum growth rate scales with the size of the colony. However, in small colonies, growth occurs throughout the colony due to the greater substrate availability. This allows for large growth rates in areas far from the peak and creates the effect in Figure 10.

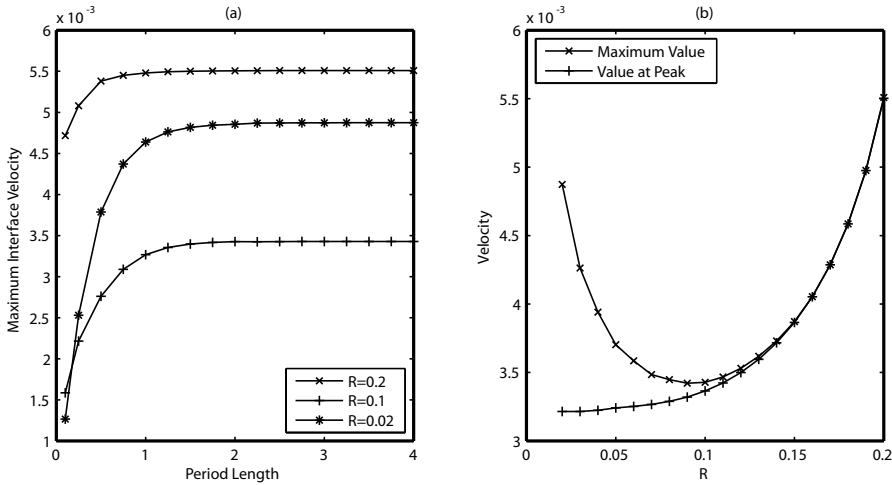


Figure 10. Selected natural growth rates. (a) The maximum growth rate for each colony size is reached on a domain with a relatively small period. (b) While the velocity at the peak decreases monotonically with colony size, the maximum velocity begins to increase again for the smallest colonies. This effect is caused by mushrooming.

Once the natural growth rate for each colony size has been found, it is possible to quantify the shadowing that takes place in the combined system. For each colony size and period length, the maximum growth rate can be expressed as a percentage of the natural rate for that colony. Figure 11 shows this ratio for each colony size, plotted against the length of the period. Using this data, it is then possible to create pictures of the “shadow” for a given influence percentage. For example, the portrait of a 50% influence shadow is shown in Figure 12. In the center of the figure is the large colony, surrounded by colonies placed so that their maximum growth rate is 50% of their natural rate. The tops of the colonies are connected to create a shadow region. Any colony which is contained within this shadow region will grow at a maximum of 50% of its natural rate. Of particular interest is the 97% shadow, shown in Figure 13, because rather than decaying asymptotically, the region of influence appears to have a sharp cutoff outside of which the presence of the large colony is virtually undetectable.

5. Conclusion

The eXtended Finite Element Method has already been shown to capture the location of an embedded interface without the need for a conforming mesh. This is

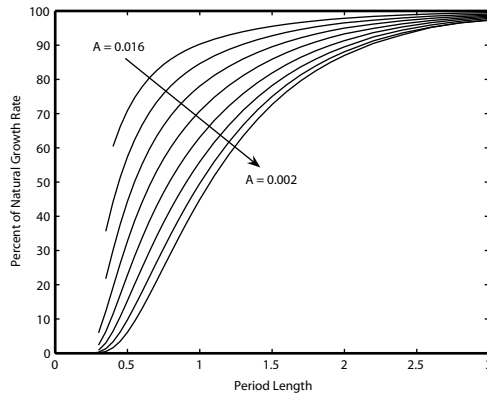


Figure 11. The effect of period length on shadowing. For all colony sizes, the shadowing effect of the large colony decreases for longer periods.

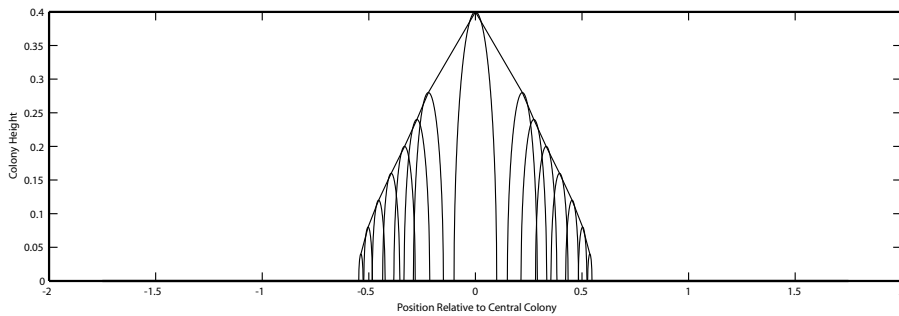


Figure 12. The 50% shadow. Any colony contained within this region around the large central colony will achieve less than 50% of its maximal growth rate.

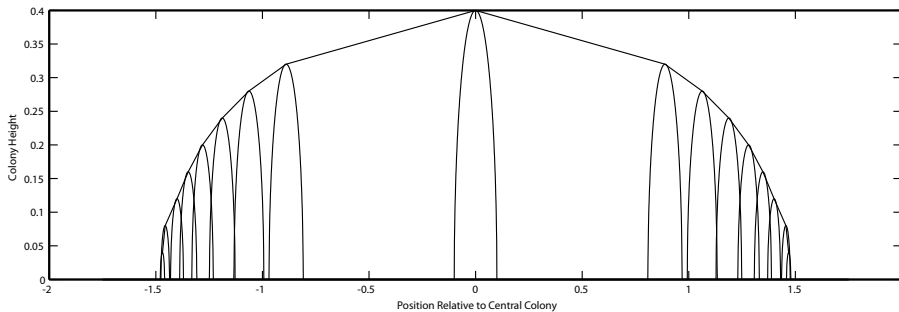


Figure 13. The 97% shadow. Any colony which falls outside of this region will achieve at least 97% of its maximal growth rate. While this shadow is significantly wider than the 50% shadow, it exhibits a steep drop off at the edges, so the effect of the central colony is largely confined to a finite area.

accomplished by adding “enriched” basis functions containing information about the interface position into the standard finite element approximation. Here we have used information about the asymptotic behavior of the solution near the interface to create customized enrichment functions which not only include the position of the interface but the boundary layer behavior of the solution as well.

The examples presented here have shown that when solutions exhibit extreme behavior in the boundary layer around the interface, the use of customized enrichment functions increases both the accuracy and the convergence rate of the numerical approximation. This is true even if the enrichment contains only the asymptotic approximation of the boundary layer behavior rather than the exact solution. While all of the problems presented here are in two dimensions, the method, including the customized enrichment functions, can be extended to three dimensions.

We then used this technique to simulate the growth of bacterial colonies in a thin film. In solving the linearized biofilm equations we have explored the relationship between the shape of the colony and the profile of its growth. The simulations have shown that the radius of curvature at the peak of the colony is the dominant factor in determining whether tip-splitting will occur as well as demonstrating that large colonies within a biofilm create a large but finite area of influence in which the growth of smaller colonies is inhibited.

References

- [1] W. G. Characklis and K. C. Marshall, *Biofilms*, Wiley, 1990.
- [2] J. Chessa and T. Belytschko, *An extended finite element method for two-phase fluids*, Transactions of the ASME **70** (2003), 10–17.
- [3] J. Chessa et al., *The extended finite element method (xfem) for solidification problems.*, International Journal of Numerical Methods in Engineering **53** (2002), 1959–1977.
- [4] D. L. Chopp, *Simulation of biofilms using the level set method*, Parametric and geometric deformable models: an application in biomaterials and medical imagery, Springer, 2006.
- [5] D. L. Chopp, M. J. Kirisits, B. Moran, and M. R. Parsek, *The dependence of quorum sensing on the depth of a growing biofilm*, Bulletin of Mathematical Biology **65** (2003), 1053–1079.
- [6] J. Dockery and I. Klapper, *Finger formation in biofilm layers*, SIAM J. Appl. Math. **62** (2001), no. 3, 853–869.
- [7] J. E. Dolbow, N. Moës, and T. Belytschko, *Discontinuous enrichment in finite elements with a partition of unity method*, Finite Elements in Analysis and Design **36** (2000), 235–260.
- [8] ———, *An extended finite element method for modeling crack growth with frictional contact*, Computational Methods in Applied Mechanics and Engineering **190** (2001), 6825–6846.
- [9] F. Gibou, R. Fedkiw, L. Cheng, and M. Kang, *A second-order-accurate symmetric discretization of the poisson equation on irregular domains*, Journal of Computational Physics **176** (2002), 205–227.
- [10] H. Ji, D. Chopp, and J. E. Dolbow, *A hybrid extended finite element/level set method for modeling phase transformation*, International Journal of Numerical Methods in Engineering **54** (2002), 1209–1233.

- [11] H. Johansen and P. Colella, *A cartesian grid embedded boundary method for poisson's equation on irregular domains*, Journal of Computational Physics **147** (1998), 60–85.
- [12] B. L. V. Jr., B. G. Smith, and D. L. Chopp, *A comparison of the extended finite element method for elliptic equations with discontinuous coefficients and singular sources*, Communications in Applied Mathematics and Computational Science **1** (2006), no. 1, 207–228.
- [13] J. S. Langer, *Instabilities and pattern formation in crystal growth*, Review of Modern Physics **52** (1980), no. 1, 1–28.
- [14] R. J. LeVeque and Z. Li, *The immersed interface method for elliptic equations with discontinuous coefficients and singular sources*, SIAM Journal Numerical Analysis **31** (1994), 1019–1044.
- [15] J. M. Melenk and I. Babuška, *The partition of unity finite element method: basic theory and applications*, Computational Methods in Applied Mechanics and Engineering **139** (1996), 289–314.
- [16] N. Moës, J. Dolbow, and T. Belytschko, *A finite element method for crack growth without remeshing*, International Journal of Numerical Methods in Engineering **46** (1999), 131–150.
- [17] S. Osher and J. A. Sethian, *Fronts propagating with curvature-dependent speed: algorithms base on hamilton-jacobi formulations*, Journal of Computational Physics **79** (1988), 12–49.
- [18] M. Stolarska, D. L. Chopp, N. Moës, and T. Belytschko, *Modelling crack growth by level sets in the extended finite element method*, International Journal of Numerical Methods in Engineering **51** (2001), 943–960.
- [19] N. Sukumar, D. Chopp, N. Moës, and T. Belytschko, *Modeling holes and inclusions by level sets in the extended finite element method*, International Journal of Numerical Methods in Engineering **48** (2000), 1549–1570.
- [20] N. Sukumar, D. L. Chopp, and B. Moran, *Extended finite element method and fast marching method for three-dimensional fatigue crack propagation*, Engineering Fracture Mechanics **70** (2003), 29–48.
- [21] G. J. Wagner, N. Moës, W. K. Liu, and T. Belytschko, *The extended finite element method for rigid particles in stokes flow*, International Journal of Numerical Methods in Engineering **51** (2001), 293–313.

Received July 8, 2006.

BRYAN G. SMITH: b-smith7@northwestern.edu
ESAM Department, Northwestern University, 2145 Sheridan Road, Evanston, IL 60208,
United States

BENJAMIN L. VAUGHAN JR.: b-vaughan@northwestern.edu
ESAM Department, Northwestern University, 2145 Sheridan Road, Evanston, IL 60208,
United States

DAVID L. CHOPP: d-chopp@northwestern.edu
ESAM Department, Northwestern University, 2145 Sheridan Road, Evanston, IL 60208,
United States